PHYSICAL REVIEW B VOLUME 5, NUMBER 2 15 JANUARY 1972

Analysis of Low-Energy Electron Diffraction from the (100), (110), and (111) Faces of Aluminum†

G. E. Laramore
Sandia Laboratories, Albuquerque, New Mexico 87115

and

C. B. Duke
Department of Physics, Materials Research Laboratory and Coordinated Science Laboratory, University of Illinois, Urbana, Illinois 61801

(Received 6 July 1971)

Experimental low-energy–electron-diffraction (LEED) intensity profiles from the (100), (110), and (111) faces of clean aluminum are analyzed using a version of the inelastic-collision model which incorporates the effects both of lattice vibrations and of a "realistic" model of the electron–ion-core potential as described by its $l \leq 2$ partial-wave phase shifts. The data consists of specular and nonspecular beams in the energy range 0–180 eV for angles of incidence between 0° and 25°. Treating the surfaces as if they were simply truncations of the bulk solid provides an adequate qualitative description of the data from Al (100) and Al (111). Analysis of the data from Al (110) suggests a contraction of the upper-layer spacing by about 10%. The failure of the calculations to describe the fine structure in the observed intensities for large angles of incidence is attributed to uncertainties in our model of the electron-solid force law.

I. INTRODUCTION

In this paper we use the finite-temperature version[1,2] of the inelastic-collision model to analyze experimental[3–7] low-energy–electron-diffraction (LEED) data from Al (100), Al (110), and Al(111). The electron–ion-core elastic scattering amplitude is specified in terms of energy-dependent phase shifts obtained from a potential constructed by Snow.[8] In spite of the relatively large electron energies 10 eV $\lesssim E \lesssim$ 200 eV, Snow's augmented-plane-wave (APW) potential, originally constructed to describe the energy-band structure of aluminum, appears to describe LEED intensity profiles for aluminum as well as potentials that have been constructed especially for the LEED energy range.[9,10]

A contemporary issue in the theory of LEED is a philosophical one concerning its objectives. In the customary view, as expressed by the authors of several recent model calculations,[10–12] one regards the goal of such a theory as the construction of a microscopic model, analogous to the energy-band model of solids, which describes observed LEED intensities in detail. In an alternative view,[13] it is recognized that the achievement of such an objective may prove to be an unusually elusive task because of our current ignorance of the detailed form of the electron-solid force law; an ignorance caused in large measure by the strong-interaction many-electron nature of this force law. Confronted with a poorly characterized force law, it initially seemed sensible to pursue an alternative objective of examining simple "schematic" models in order to discover which of their predictions are sensitive to the various aspects of this force law. In this spirit, our previous analyses[2,13–17] of experimental LEED intensities were based on a simplified version of the inelastic-collision model in which energy-independent s-wave phase shifts were used to parametrize a schematic electron–ion-core interaction.

In these earlier isotropic-scatterer "schematic" model studies we established certain features of the model calculations which appear to be independent of the details of the electron-solid force law.[13–16] We now turn our attention to the next step in our program of analyzing elastic LEED intensities— the construction of a model of LEED from aluminum incorporating a microscopic model of the electron–ion-core interaction and the examination of the extent to which it adequately describes those features of the data which are (sensitive) indicators of the detailed form of this force law. To this end we provide an analysis of a rather large block of experimental data: intensity profiles for angles of incidence $0° \leq \theta \leq 25°$ for both specular and nonspecular beams on three different faces of the same material. The consideration of such a large quantity of data is essential because some of the limitations of the model become apparent only when the intensities obtained for wide ranges of incident angle and a variety of crystal faces are analyzed using the same electron-solid interaction.

Our earlier isotropic-scatterer model analyses of experimental LEED intensity profiles from Al (100) and Al (110) led to three discrepancies between the model predictions and the experimental data.[13,14] We show in this paper that two of these, the failure of the isotropic-scatterer model to predict the changes in scattered intensity as a function of angle of incidence and its failure to provide enough fine structure between the prominent maxima near the kinematical Bragg energies, are remedied by the use of a more accurate short-range electron–ion-core potential. However, even Snow's more refined model potential as used herein (or the analogous potential of Tong and Rhodin[9,10]) fails to describe adequately the fine structure in the observed intensity profiles for large angles of incidence. The third discrepancy noted earlier,[9,14] the need to use different inner potentials for the (100) ($V_0 = 16.7$ eV) and (110) ($V_0 \cong 0$) faces of aluminum, remains in the present refined version of the model. In particular, we find that the (110) face of aluminum exhibits intensity profiles with peaks located 10 – 15 eV higher in energy than expected on the basis of model calculations which place peaks within about 5 eV of their observed positions for intensity profiles from Al (100) and Al (111). This is somewhat surprising since lattice-dynamics calculations based upon two-body force models predict an expansion of the upper-layer spacing for all three faces with the upper-layer spacing of the (110) face having the largest percentage of expansion.[18,19] An expansion of the upper-layer spacing would have the effect of shifting the peak positions to lower- rather than to higher-energy values.[14] Therefore the experimental data seem to suggest that the upper-layer spacing for Al (110) is contracted instead of expanded relative to the bulk-layer spacing. Because of uncertainties in the magnitude and angular dependence of the inner potential, it is not possible to extract precise quantitative information about absolute contractions or expansions in the upper-layer spacings. However, provided that the faces in question are reasonable approximations to chemically clean idealized surfaces, the inner potential should be approximately equal (to within a few eV) for all three faces. Thus it is possible to compare the consequences of relative changes in the upper-layer spacings between different faces of the same material. Perhaps it should be noted that since for the data analyzed herein there was no independent monitor of surface cleanliness, such as Auger[20] or appearance potential spectroscopy,[21] the chemical condition of the surfaces involved was not precisely characterized. However, to the extent that these data are representative of clean idealized single-crystal faces, the failure of our microscopic model to predict the fine structure in the intensity profiles at large angles of incidence, the variation in inner potential from one crystal face to another, and its occasional variation from one beam to another for a given crystal face is interpreted by us as further indications of the poorly known character of the details of the electron-solid force law or of the topological features of the solid surface, and the concomitant inadequacy of simple models thereof.

In Sec. II, we review the definition of the finite-temperature inelastic-collision model and discuss the use of reflectivity boundary conditions[22] in order to obtain an absolute reflectivity from the calculation (rather than a cross section as in earlier work).[13-17] We then apply the model to calculate intensity profiles from Al (100), Al (110), and Al (111) in Secs. III, IV, and V, respectively. In Sec. IV, we enumerate ways in which a "chemically clean" surface region can be inequivalent to the bulk region and discuss how these inequivalences can affect the LEED profiles. Finally, in Sec. VII, we summarize our results.

II. DEFINITION OF MODEL

The detailed definition of the finite-temperature inelastic-collision model has been given elsewhere.[1,2] Therefore we simply recall some of the relevant equations and present the minor extensions necessary to specify our treatment of higher partial-wave phase shifts and to use reflectivity boundary conditions[22] rather than scattering boundary conditions.[1]

The cross section is given by

$$\frac{d^2\sigma}{dE\,d\Omega}\bigg|_{\substack{\vec{k}_i\to\vec{k}_f\\ \text{elastic}}} = \left(\frac{m}{2\pi\hbar^2}\right)^2 \delta(E_i - E_f)\,|\,I(\vec{k}_f,\vec{k}_i)|^2, \tag{2.1}$$

$$I(\vec{k}_f,\vec{k}_i) = \frac{(2\pi)^2}{A}\sum_{\lambda}\sum_{\vec{g}} \exp[-i(k_{f\perp}-k_{i\perp})d_\lambda - i\vec{g}\cdot\vec{a}_\lambda] \times T_\lambda(\vec{k}_f,\vec{k}_i)\;\delta(\vec{k}_{f\parallel}-\vec{k}_{i\parallel}-\vec{g}). \tag{2.2}$$

The subscripts i and f label, respectively, the initial and final states of the scattered electron; T_λ is the amplitude for all scattering processes where the final scattering event takes place in the λth subplane; d_λ is the perpendicular distance of the λth subplane from the surface; $\vec{a}_\lambda$ is the translational displacement of the λth subplane relative to a reference point on the surface; $\vec{g}$ is a reciprocal-lattice vector characterizing the two-dimensional periodicity of the system; A is the area of a unit cell; and the subscripts $\parallel$ and $\perp$ are defined relative to the surface of the crystal. The amplitude T_λ is expanded in terms of partial waves according to

$$T_\lambda(\vec{k}_f,\vec{k}_i) = \sum_{LL'} T_\lambda^{LL'}[k(E)]\,Y_L^*(\Omega_f)\,Y_{L'}(\Omega_i). \tag{2.3}$$

It is related to the partial-wave components of the effective electron–ion-core scattering amplitude through the following matrix equation:

$$T_\lambda^{LL'}[k(E)] = \tau_\lambda^{LL'}[k(E)] + \sum_{L_1L_2}\sum_{\lambda_1\neq\lambda} \tau_\lambda^{LL'}[k(E)]\,G_{L_1L_2}^{\lambda\lambda_1}(\vec{k}_i) \times T_{\lambda_1}^{L_2L'}[k(E)], \tag{2.4a}$$

$$\tau^{LL'}_{\lambda}[k(E)] = b^{LL'}_{\lambda}[k(E)] + \sum_{L_1 L_2} b^{LL_1}_{\lambda}[k(E)]\, G^{SP}_{L_1 L_2}(\vec{k}_i) \times \tau^{L_2 L'}_{\lambda}[k(E)]. \tag{2.4b}$$

In Eqs. (2.3) and (2.4), the

$$Y_L(\Omega) \equiv Y_{l,m}(\Omega) \tag{2.5}$$

are the spherical harmonic functions,[23]

$$\sum_L = \sum_l \sum_{m=-l}^{l} , \tag{2.6}$$

and the $b^{LL'}_{\lambda}$ are the partial-wave components of the effective electron–ion-core scattering amplitude for an ion core in the λth subplane. With the exception of the $b^{LL'}_{\lambda}$ (which will be discussed later in this section), the reader is referred to Ref. 2 for the definition of the quantities in Eqs. (2.3) and (2.4). The $G_{LL'}$ are propagators which may be written in terms of the one-electron Green's function $G(\vec{k}, E)$ for a uniform interacting electron fluid. We assume that it is spherically symmetrical and that the electronic proper self-energy $\Sigma(\vec{k}, E)$ depends only on E:

$$G(k, E) = \left(E - \frac{\hbar^2 k^2}{2m} - \Sigma(E)\right)^{-1} \equiv \frac{2m/\hbar^2}{k^2(E) - k^2} , \tag{2.7}$$

$$k^2(E) = E - \Sigma(E). \tag{2.8}$$

Equation (2.8) specifies the $k(E)$ used in $T^{LL'}_{\lambda}[k(E)]$.

We wish to relate

$$R_{\vec{g}}(\vec{k}_f, \vec{k}_i) \equiv \sum\nolimits_{\lambda} \exp[-i(k_{f\perp} - k_{i\perp})d_{\lambda} - i\vec{g}\cdot\vec{a}_{\lambda}] \times T_{\lambda}(\vec{k}_f, \vec{k}_i) \tag{2.9}$$

to the reflectivity of the gth beam. This is accomplished by considering the definition of the scattered wave function in the coordinate representation

$$\psi^{+}_{i}(\vec{r}) = \frac{e^{i\vec{k}_i\cdot\vec{r}}}{(2\pi)^{3/2}} + \int (dr_1)\,(dr_2)\, G(\vec{r} - \vec{r}_1) \times T(\vec{r}_1, \vec{r}_2)\, \frac{e^{i\vec{k}_i\cdot\vec{r}_2}}{(2\pi)^{3/2}} . \tag{2.10}$$

In writing Eq. (2.10) we have taken a plane-wave basis set in describing the scattering process[24] and have normalized the volume of the system to unity.

The Green's function in Eq. (2.10) is the coordinate space representation of Eq. (2.7), i.e.,

$$G(\vec{r} - \vec{r}_1) = \int \frac{(dk)}{(2\pi)^3}\, e^{i\vec{k}\cdot(\vec{r}-\vec{r}_1)} G(\vec{k}, E) . \tag{2.11}$$

The scattering matrix $T(\vec{r}_1, \vec{r}_2)$ is the coordinate-space form of the quantity $I(\vec{k}_1, \vec{k}_2)$ that determines the scattering cross section[24]

$$T(\vec{r}_1, \vec{r}_2) = \int \frac{(dk_1)\,(dk_2)}{(2\pi)^6}\, e^{i\vec{k}_1\cdot\vec{r}_1 - i\vec{k}_2\cdot\vec{r}_2}\, I(\vec{k}_1, \vec{k}_2) . \tag{2.12}$$

Substituting Eqs. (2.11) and (2.12) into Eq. (2.10) we obtain

$$\psi^{+}_{i}(\vec{r}) = \frac{e^{i\vec{k}_i\cdot\vec{r}}}{(2\pi)^{3/2}} + \int \frac{(dk)}{(2\pi)^{9/2}}\, G(\vec{k}, E)\, e^{i\vec{k}\cdot\vec{r}}\, I(\vec{k}, \vec{k}_1) . \tag{2.13}$$

Using the form of $I(\vec{k}, \vec{k}_1)$ for a semi-infinite periodic system which is given in Eq. (2.2) we obtain

$$\psi^{+}_{i}(\vec{r}) = \frac{e^{i\vec{k}_i\cdot\vec{r}}}{(2\pi)^{3/2}} - \frac{2m}{\hbar^2 A} \sum_{\vec{g}} \int \frac{dk_\perp}{(2\pi)^{5/2}} \times \frac{\exp[i(\vec{k}_{i\parallel} + \vec{g} + k_\perp \hat{z})\cdot\vec{r}]\, R_{\vec{g}}(\vec{k}_{i\parallel} + \vec{g} + k_\perp\hat{z}, \vec{k}_i)}{k_\perp^2 - k_\perp^2(\vec{g}, E)} , \tag{2.14}$$

$$k_\perp^2(\vec{g}, E) = k^2(E) - (\vec{k}_{i\parallel} + \vec{g})^2. \tag{2.15}$$

The integral over $k_\perp$ can be done by contour integration. The half-plane in which the contour is closed is determined by the sign of z. We take the solid to lie in the half-space $z > 0$ and consider the wave function only in this region. We assume implicitly that all of the electronic wave function is transmitted through the plane at $z = 0$ and that any reflection is due to interaction between the electrons and the ion cores.[1,2,12–17] The effect of an explicit reflection at the surface of the solid has been considered by Jepson *et al.*[25] They also conclude that the "no reflection" boundary condition is the most reasonable. This is physically sensible since the electron-solid potential extends to long distances outside the solid in the form of the image force so no abrupt discontinuity in the electron-solid potential occurs at the surface of the solid. The use of this boundary condition is introduced to avoid the difficult problem of actually determining the electron-solid force in the surface region.[26,27] The fact that it produces the correct order of magnitude for the intensity profiles[9] suggests that it contains much of the essential physics.

Using this procedure we have to consider only the singularities of the integrand of Eq. (2.15) that lie in the upper half $k_\perp$ plane. There are two classes of singularities: (a) the pole in the Green's function at

$$\bar{k}_\perp(\vec{g}, E) = \mathrm{Re}\,k_\perp(\vec{g}, E) + i\,\mathrm{Im}\,k_\perp(\vec{g}, E) , \tag{2.16}$$

which produces a scattering term[28] and (b) the singularities in R which produce bound-state terms.

We only consider the scattering term in determining the reflected wave function since the scattered electrons are observed at distances far from the crystal. Hence we obtain for this wave function

$$\psi_i^+(\vec{r}) = \frac{e^{i\vec{k}_i\cdot\vec{r}}}{(2\pi)^{3/2}} - \frac{mi}{\hbar^2 A} \times \sum_{\vec{g}} \frac{\exp[i(\vec{k}_{i\parallel} + \vec{g} + \vec{k}_\perp(\vec{g},E)\hat{z})\cdot\vec{r}]}{(2\pi)^{3/2}\tilde{k}_\perp(\vec{g},E)} \times R_{\vec{g}}(\vec{k}_{i\parallel} + \vec{g} + \tilde{k}_\perp(\vec{g},E)\hat{z}, \vec{k}_i) \, . \quad (2.17)$$

The function

$$\chi_f(\vec{g}) = \frac{\exp[i(\vec{k}_{i\parallel} + \vec{g} + \tilde{k}_\perp(\vec{g},E)\hat{z})\cdot\vec{r}]}{(2\pi)^{3/2}} \quad (2.18)$$

is the part of the wave function inside the solid that becomes the plane-wave state

$$\phi_f = \frac{e^{i\vec{k}_f\cdot\vec{r}}}{(2\pi)^{3/2}} \, , \quad (2.19)$$

$$\vec{k}_{f\parallel} = \vec{k}_{i\parallel} + \vec{g} \quad (2.20)$$

outside the solid. Thus we interpret

$$R(\vec{g},E) = \frac{-mi\, R_{\vec{g}}(\vec{k}_{i\parallel} + \vec{g} + \tilde{k}_\perp(\vec{g},E)\hat{z}, \vec{k}_i)}{\hbar^2 A \tilde{k}_\perp(\vec{g},E)} \quad (2.21)$$

as the reflection amplitude associated with the *g*th beam.

Ideally, the experimentally measured quantity is the reflectivity

$$I(\vec{g}) = \frac{J_{\text{out}}}{J_{\text{in}}} = \frac{k_\perp^{\text{ext}}(\vec{g},E)}{k_\perp^{\text{ext}}(0,E)} \, |R(\vec{g},E)|^2 \, , \quad (2.22)$$

where J_{in} and J_{out} are, respectively, the incident current per unit area and the reflected current per unit area of the *g*th beam. In Eq. (2.23), the $k_\perp^{\text{ext}}$ are determined external to the crystal. They represent normalization factors which take into account the change in the effective area with beam angle, i.e.,

$$k_\perp^{\text{ext}}(\vec{g},E) = [(2m/\hbar^2)\, E - (\vec{k}_{i\parallel} + \vec{g})^2]^{1/2} \, . \quad (2.23)$$

Comparison of Eqs. (2.1) and (2.23) shows that it is elementary to change from a calculation of the scattering cross section to a calculation of the reflectivity. $I(\vec{g})$ is the quantity that is calculated in this paper. It only remains to specify the effective electron–ion-core elastic scattering vertex and the self-energy $\Sigma(E)$ used in the electron propagator.

The effective finite-temperature electron–ion-core elastic scattering vertex is given by[1,2]

$$b_n(\vec{k}_2, \vec{k}_1) = e^{-W_n(\vec{k}_2 - \vec{k}_1)}\, t_n(\vec{k}_2, \vec{k}_1) \, , \quad (2.24)$$

$$W_n(\vec{k}_2 - \vec{k}_1) = \tfrac{1}{2}(k_2 - k_1)^\alpha \langle u_n^\alpha u_n^\beta \rangle_T (k_2 - k_1)^\beta \, , \quad (2.25)$$

in which $t_n(\vec{k}_2, \vec{k}_1)$ is the scattering amplitude for *n*th ion core when it is held rigid. In Eq. (2.26), u_n^α is the αth component of the displacement from equilibrium of the *n*th ion core. We use the convention of summing over repeated Cartesian indices. Using the Debye model[29] of the phonon spectrum of the solid to evaluate Eq. (2.25), we obtain[1]

$$W_n(\vec{q}) = \frac{3\hbar^2 q^2}{2M_n k_B \Theta_D^n} \left[\frac{1}{4} + \left(\frac{T}{\Theta_D^n} \right)^2 \int_0^{\Theta_D^n/T} dx \frac{x}{e^x - 1} \right] \, , \quad (2.26)$$

where M_n is the mass of the *n*th ion core and Θ_D^n is an effective Debye temperature that describes the amplitude of its vibration. Although it is generally accepted that the surface ions have a larger amplitude of vibration than the "bulk" ions,[18,19,30–32] in the absence of precise data on these amplitudes we simply assume all of the ion cores to have an amplitude of vibration characterized by the "bulk" value[33] of

$$\Theta_D = 426\ {}^\circ\text{K}. \quad (2.27)$$

Since all of the measurements considered here are presumably at room temperature, we expect the model prediction to be insensitive to this choice.[2,14] The effects on the LEED profiles of a larger amplitude of vibration for the surface ions have been investigated.[2] Provided that the lattice constants are held fixed, the primary effect is simply to reduce the heights of peaks in the intensity profiles. However, the amount of reduction increases with the energy of the peak—a fact which should be kept in mind when comparing the calculated intensity profiles with experimental measurements. One also should recall that much of the experimental data[3,4,6] was taken with a fluorescent screen-photometer combination. Hence it is not clear the degree to which electrons that have inelastically scattered from phonons are included in the angular acceptance of the detector. The inclusion of these electrons in the experimental measurement would have the effect of increasing the experimental peaks relative to the theoretical peaks. Unless one is going to analyze data taken over a wide temperature range, there appears to be no reason to go beyond the simple model specified by Eqs. (2.26) and (2.27).

The scattering amplitude for the rigid ion core is specified in terms of energy-dependent phase shifts obtained from the APW band-structure potential of Snow.[8] The first four phase shifts obtained from this potential[34] are shown in Fig. 1. Because of computational time limitations, only the *s*-, *p*-, and *d*-wave phase shifts were used in the calculation. The relative magnitudes of the phase shifts indicate that there should be no appreciable error caused by neglect of the *f* and higher-order phase shifts below about 100 eV. Work using still more partial waves ($l \le 8$) indicates that the only changes occurring above 100 eV are in the details of the secondary structure.[25] As the inclusion of $l \le 8$ partial waves makes the analysis of large amounts of data considerably more expen-

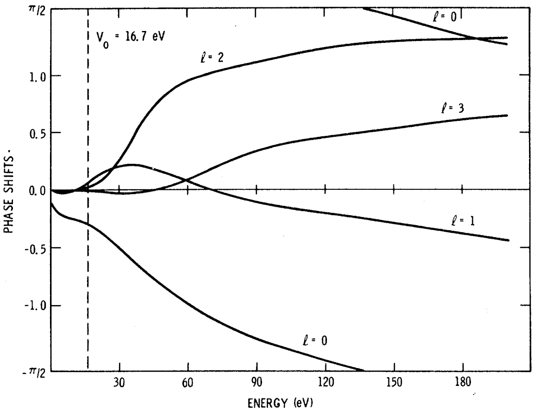

FIG. 1. Phase shifts obtained from the APW potential of Snow (Ref. 8). The energy scale is measured relative to the constant value of the potential between the muffin-tin potentials. This zero level is 16.7 eV below the vacuum level and so a zero-energy electron outside the crystal will have $V_0 = 16.7$ eV energy when it has entered the solid. The dotted line at 16.7 eV indicates the zero level for external electron energies measured relative to the vacuum.

sive, using $l \leq 2$ seems to us to be a reasonable compromise as far as using a "realistic" model of the electron–ion-core potential for Al in the energy range $0 \leq E \leq 180$ eV.

We proceed by obtaining the first three partial-wave components of the effective electron–ion-core elastic scattering amplitude via

$$b_n(\vec{k}_2 - \vec{k}_1) = e^{-W_n(\vec{k}_2 - \vec{k}_1)} \sum_{l'} \frac{2l'+1}{4\pi} t_n^{l'}(k) P_{l'}(\cos\theta_{12})$$

$$\equiv \sum_l b_n^l(k) \frac{2l+1}{4\pi} P_l(\cos\theta_{12}) , \tag{2.28}$$

$$|\vec{k}_1| = |\vec{k}_2| = k = \left(\frac{2m}{\hbar^2}(E + V_0)\right)^{1/2} , \tag{2.29}$$

$$t_n^l(k) = \frac{4\pi^2 i\hbar^2}{mk} \left(e^{2i\delta_l^n(k)} - 1\right) . \tag{2.30}$$

θ_{12} is the angle between $\vec{k}_1$ and $\vec{k}_2$, E is the electron energy measured external to the solid, and $W_n(\vec{k}_2 - \vec{k}_1)$ is given by Eq. (2.26). The expansion of b_n in terms of the $P_l(\cos\theta_{12})$ in Eq. (2.28) is a direct consequence of the assumed spherically symmetric mode of vibration of the ion cores. The matrices $b_n^{LL'}$ used in Eq. (2.4b) are diagonal for the special case of a spherically symmetric effective electron–ion-core elastic scattering vertex. The diagonal elements are the b_n given in Eq. (2.28).

$$b_n^{LL'}(k) = b_n^l(k)\, \delta_{LL'} . \tag{2.31}$$

The b_n^l are obtained from Eq. (2.28)

$$b_n^l(k) = 2\pi e^{-2k^2\overline{W}_n} \sum_{l'} \frac{2l'+1}{4\pi} t_n^{l'}(k) \int_0^\pi d\theta \, \sin\theta$$

$$\times e^{2k^2\overline{W}_n \cos\theta} P_{l'}(\cos\theta) P_l(\cos\theta) , \tag{2.32}$$

$$\overline{W}_n = \frac{3\hbar^2}{2M_n k_B \Theta_D^n}\left[\frac{1}{4} + \left(\frac{T}{\Theta_D^n}\right)^2 \int_0^{\Theta_D^n/T} dx \frac{x}{e^x - 1}\right]. \tag{2.33}$$

For $l = 0, 1, 2$ we find the following explicit forms:

$$b_n^{(0)}(k) = \tfrac{1}{2} e^{-A} \{t_n^{(0)}(k) I_0(A) + 3t_n^{(1)}(k) I_1(A)$$
$$+ \tfrac{5}{2} t_n^{(2)}(k) [3I_2(A) - I_0(A)]\}, \tag{2.34a}$$

$$b_n^{(1)}(k) = \tfrac{1}{2} e^{-A} \{t_n^{(0)}(k) I_1(A) + 3t_n^{(1)}(k) I_2(A)$$
$$+ \tfrac{5}{2} t_n^{(2)}(k) [3I_3(A) - I_1(A)]\} , \tag{2.34b}$$

$$b_n^{(2)}(k) = \tfrac{1}{2} e^{-A} \{t_n^{(0)}(k) [\tfrac{3}{2} I_2(A) - \tfrac{1}{2} I_0(A)]$$
$$+ 3t_n^{(1)}(k) [\tfrac{3}{2} I_3(A) - \tfrac{1}{2} I_1(A)]$$
$$+ \tfrac{5}{2} t_n^{(2)}(k) [\tfrac{9}{2} I_4(A) - 3I_2(A) + \tfrac{1}{2} I_0(A)]\} , \tag{2.34c}$$

where

$$A = 2\overline{W}_n k^2 , \tag{2.35}$$

$$I_0(A) = 2(\sinh A)/A , \tag{2.36a}$$

$$I_0(A) = \left(\frac{\partial}{\partial A}\right)^j I_0(A). \tag{2.36b}$$

Equations (2.28)–(2.31) and (2.34) specify our model of the effective electron–ion-core elastic scattering vertex in terms of the phase shifts obtained from Snow's potential[8] and a single effective Debye temperature.[29]

The real part of the electronic self-energy in our model also is determined from Snow's potential.[8] It is the difference in energy between the vacuum and the value of the constant potential between the muffin tins

$$\mathrm{Re}\, \Sigma(E) = -V_0 = -16.7 \text{ eV}. \tag{2.37}$$

We regard this choice as both necessary and unique because we must define the electron–ion-core interaction energy and the electron–conduction-electron interaction energy relative to the same energy zero which ultimately must be referred to the vacuum level. Other workers[10,25] do not impose this consistency requirement but rather determine the energy zeros for the electron–ion-core interactions and the electronic proper self-energy $\Sigma(E)$ independently.

The only "adjustable" parameter in our calculation is the characteristic mean free path for energy loss by the beam electrons in the solid. This parameter determines $\mathrm{Im}\,\Sigma(E)$ through

$$\mathrm{Im}\, \Sigma(E) = -\left(\frac{\hbar^2}{m\lambda_{ee}}\right)\left(\frac{2mE}{\hbar^2} + \frac{2mV_0}{\hbar^2}\right)^{1/2} , \tag{2.38}$$

where λ_{ee} is twice the effective electron mean free path. In practice λ_{ee} is energy dependent, but estimates of its value have been made only for in-

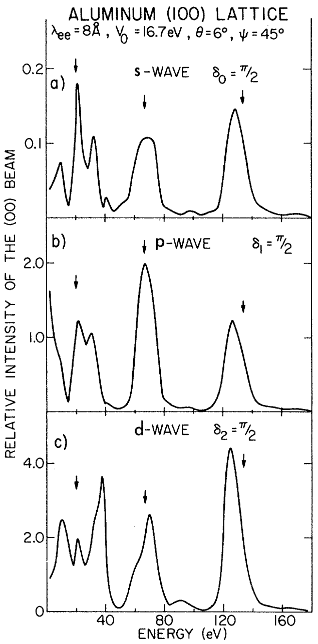

FIG. 2. Effect of higher partial waves upon the calculated intensity profiles. The panels of the figure show intensity profiles calculated for *s*-, *p*-, and *d*-wave scatterers placed in an Al (100) lattice structure. The strength of the scatterers is at the unitary limit in each case. The polar angle is denoted by θ and the azimuthal angle by ψ. ψ is measured relative to the nonprimitive cubic unit cell axes (Ref. 3). The parameters used in the calculation are shown in the figure. The arrows mark the kinematical positions of the Bragg peaks for an inner potential of 16.7 eV. The scales on the ordinates indicate the relative values of the scattering cross section.

finite electron-gas systems.[10,12,15] It is not clear how valid these estimates are for the case of LEED where the electron is confined to the surface region of a real material and surface effects are important in determining λ_{ee}. Instead of using an energy dependent λ_{ee}, we simply take it to have the constant value

$$\lambda_{ee}=8\ \text{Å}\ , \tag{2.39}$$

which seems reasonable on the basis of earlier work in aluminum.[13–17] In the energy range which we are considering, this model becomes inadequate only for electron energies below ~ 25 eV, where 8 Å is probably too small a value. Larger values of λ_{ee} would have the effect of increasing the size of the peaks in the calculated intensity profiles.[13,15]

We solve the matrix equations (2.4) for a finite number of layers and evaluate either the elastic scattering cross sections [Eq. (2.1)] or the reflectivity [Eq. (2.22)]. Enough layers are taken to ensure a good approximation to a semi-infinite solid.[16] In practice this means using at least five layers for Al (100) and Al (111) with their respective "bulk"-layer spacings of 2.0201 and 2.3326 Å and at least seven layers for Al (110) with its smaller "bulk"-layer spacing of 1.4284 Å. The lattice dimensions of aluminum were taken from Goldsmith *et al.*[35] for room temperature ($T\simeq 293$ °K).

Before closing this section it is perhaps appropriate to note the sensitivity of the various features of the LEED profiles to the form of the electron–ion-core potential. It is especially instructive to compare the effects of the various partial waves upon the profiles. This is shown in Fig. 2 where we compare the relative scattering properties of *s*-, *p*-, and *d*-wave potentials for rigid ion cores in an Al (100) lattice. Other than the phase shifts, the parameters used in the calculation correspond to those used in the aluminum intensity profile calculations. Note that all three types of scatterers place prominent peaks fairly near the kinematical Bragg positions. The positions of the higher-energy maxima near the primary Bragg energies appear particularly insensitive to details of the electron-ion-core potential. The *d* waves produce a large amount of secondary structure near 40 eV for this particular angle of incidence. This secondary structure is clearly present in the experimental profiles[3,4] but notably absent in previous *s*-wave calculations of the intensity profiles.[13–17] The increasing magnitude of the scattering with increasing l is a direct consequence of the $(2l+1)$ weighting factor in Eq. (2.28).

We now turn to calculations of intensity profiles using the phase shifts shown in Fig. 1.

III. ALUMINUM (100)

As noted in the Introduction, to adequately test the validity of a model description of LEED, it is necessary to analyze large blocks of data. As will soon become apparent, neither the experimental nor the theoretical state of the art is sufficiently advanced to allow the extraction of reliable conclusions on the basis of comparing experimental measurements and theoretical calculations for a few beam parameters. A common way of comparing experimental work with model calculations is to vary the polar angle θ for fixed azimuthal angle ψ. We concentrate on the azimuth $\psi=45°$ (relative to the nonprimitive cubic unit cell[3]) for two reasons:
(i) Previous model calculations using the phenomenological isotropic-scatterer version of the inelastic-collision model concentrated on this azimuth[14,17] and comparison of the calculated intensity profiles in this section with this previous work will allow us to directly assess the results of incorporating the higher partial waves into the calculation.
(ii) There is experimental work on both specular and nonspecular beams available for this azimuth.[3]
We take as our model of the surface simply a trun-

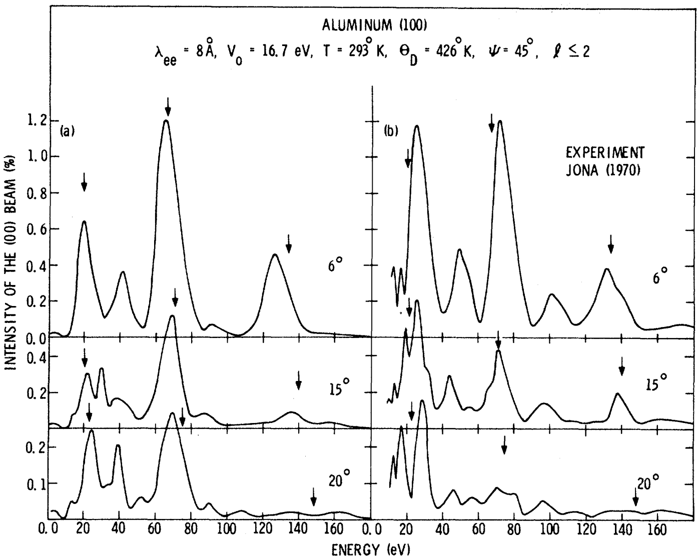

FIG. 3. Comparison between the predictions of (a) model calculations and the (b) experimental data of Jona (Ref. 3) for the (00) beam on Al (100). Curves are labeled according to the polar angle θ. The azimuthal angle ψ is measured relative to the nonprimitive cubic unit cell (Ref. 3). The parameters used in the calculation are indicated on the figure. The kinematical positions of the Bragg peaks for $V_0 = 16.7$ eV are indicated by arrows. The theoretical calculations are for the absolute reflectivity. The units of the experimental curves are arbitrary.

cated periodic bulk solid. That is, we take the surface ion cores to be electronically, vibronically, and geometrically equivalent to those in the "bulk." This model produces a reasonable description of the experimental profiles from Al (100).

In Fig. 3, we show a comparison between the results of the model calculations and Jona's experimental data for the specular beam. The experimental and theoretical positions of the predominant peaks agree to within ~5 eV. At $\theta = 6°$, the experimental peaks lie above the theoretical peaks; at $\theta = 15°$, the experimental and the theoretical peak positions nearly coincide; and at $\theta = 20°$, if anything, the experimental peaks lie at a lower energy than the theoretical peaks. At $\theta = 6°$ and 15°, there is good agreement between the features of the experimental and the theoretical profiles. However, at $\theta = 20°$, the theoretical peak near 70 eV does not exhibit the splitting evident in the experimental data. The observed systematic behavior of the low-energy peak at $\theta = 6°$, changing into a doublet with increasing θ, is evident also in the theoretical profiles. The sharp structure in the experimental profiles below 20 eV is probably due to inelastic threshold effects[13,36] which are not included in the present calculation. The theoretical calculations also underestimate the secondary structure near 100 eV although the inclusion of still more partial waves into the calculation seems to enhance this structure.[25] Perhaps the most striking result evident in the figure is the deterioration of the agreement between theory and experiment as θ increases.

In Fig. 4, we show a comparison between the results of model calculations and Jona's experi-

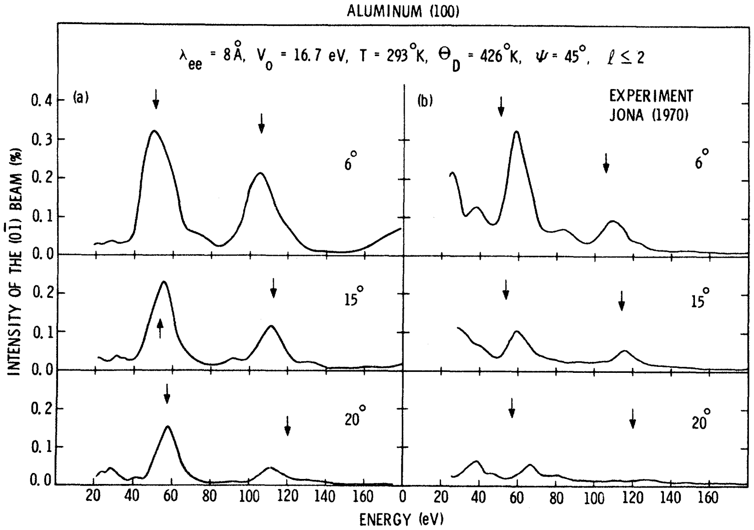

FIG. 4. Comparison between the (a) model predictions and (b) Jona's experimental data (Ref. 3) for the (0$\bar{1}$) beam. The beam is labeled according to the primitive two-dimensional unit cell as was done by Tucker and Duke (Ref. 16), not according to the nonprimitive cubic two-dimensional cell as was done by Jona (Ref. 3) $[(0\bar{1})_{TD} = (1\bar{1})_J]$. Model calculations are based on the parameters shown in the figure. The curves are labeled according to the polar angle θ. The azimuthal angle ψ is measured relative to the nonprimitive cubic cell (Ref. 5). The arrows mark the kinematical positions of the Bragg peaks using $V_0 = 16.7$ eV. The theoretical calculations are for the absolute reflectivity. The units of the experimental curves are arbitrary.

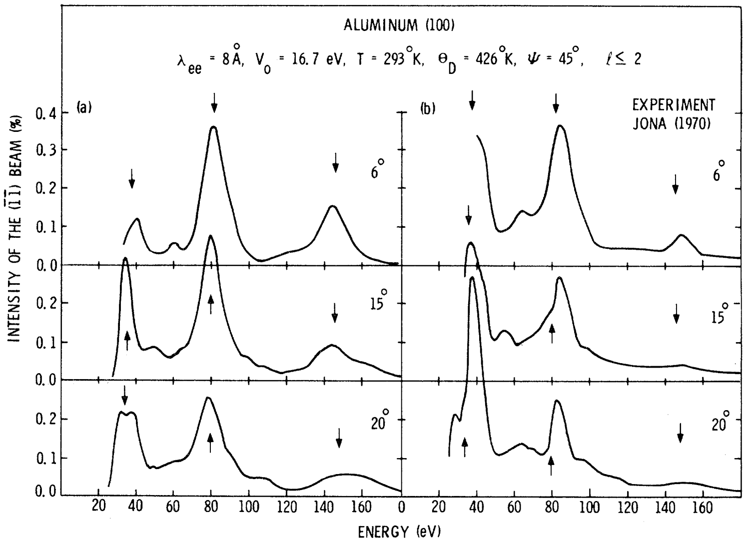

FIG. 5. Comparison between the (a) model predictions and (b) Jona's experimental data (Ref. 3) for the ($\bar{1}\ \bar{1}$) beam. The beam is labeled according to the primitive two-dimensional unit cell as was done by Tucker and Duke (Ref. 16), not according to the nonprimitive cubic two-dimensional cell as was done by Jona (Ref. 3) [$(\bar{1}\ \bar{1})_{TD} = (0\bar{2})_J$]. Model calculations are based on the parameters shown in the figure with the azimuthal angle ψ being measured relative to the nonprimitive cubic cell (Ref. 3). The curves are labeled according to the polar angle θ. The arrows mark the kinematical positions of the Bragg peaks using $V_0 = 16.7$ eV. The theoretical calculations are for the absolute reflectivity. The units for the experimental curves are arbitrary.

mental data[3] for the ($0\bar{1}$) beam. At $\theta = 6°$ and $15°$ the agreement between theory and experiment is not unreasonable although the experimental peaks lie 5–7 eV higher in energy than the theoretically predicted peak positions. At $\vartheta = 20°$ the agreement between theory and experiment is too poor to say anything about relative peak positions.

A comparison between the results of model calculations and Jona's experimental data[3] for the ($\overline{11}$) beam is shown in Fig. 5. There is good agreement between the model predictions and the experimental results for all three angles of incidence. The peaks in the theoretical curves lie within ~2 eV of the experimentally measured positions.

To assess which features of the experimental data may be regarded as common to a variety of experiments, in Fig. 6, we compare experimental data from three sources[3–5] with the predictions of model calculations. Except for Jona's work,[3] the other experimental work on Al (100) has been restricted to normal incidence. Farrell and Somorjai[4] give a curve for the (00) beam for nearly normal incidence. Comparing this with the theoretical curve for normal incidence shows excellent agreement with regard to peak position. However, the experimental data are not normalized to the incident beam current—a fact whose consequences are particularly visible at low energies. The theoretical model predicts the lowest-energy peak at 20 eV while the experimental data show the corresponding peak at 26 eV with only a shoulder at 20 eV. For the (10) and the (11) beams there is generally good agreement between the model predictions and the three sets of experiments. One thing that is noticeable in comparing the various workers' experimental data is the lack of consistency as to which member of a multiple-scattering cluster[16] of peaks near a Bragg energy is dominant, i.e., which is the peak and which is the shoulder. This is a sensitive function of the beam parameters in some cases. The effect is especially noticeable in the

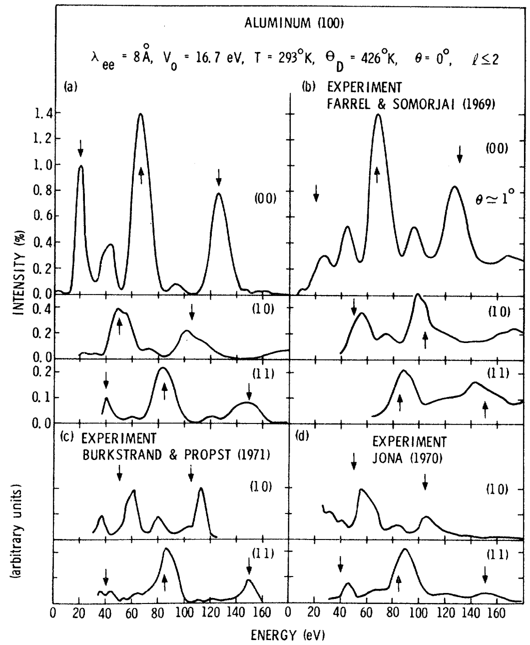

FIG. 6. Comparison between (a) the predictions of model calculations with (b) the experimental work of Farrell and Somorjai (Ref. 4), (c) Burkstrand and Propst (Ref. 5), and (d) of Jona (Ref. 3). Beams are labeled according to the primitive two-dimensional unit cell (Ref. 16). The model calculations are based on the parameters shown in the figure. The arrows mark the kinematical positions of the Bragg peaks using $V_0 = 16.7$ eV. The theoretical calculations are for the absolute reflectively. The units of the experimental curves are arbitrary.

TABLE I. Comparison between experimentally observed and theoretically predicted positions (peak positions given in eV) of the prominent peaks in the LEED profiles for the (00) beam on Al(100).

	Experimental		Theoretical		
	Ref. 3	Ref. 4	This work and Ref. 9	Ref. 25[a]	Ref. 10
$\theta = 0°$		25	20	24	20
		44	44	51	48
		67	65	77	65
		126	126	131	135
			$\Delta = 2.7$	$\Delta = 5.8$	$\Delta = 6.4$
$\theta = 6°$	25		20	24	
$\psi = 45°$	49		41	49	
	72		66	70	
	132		126	133	
			$\Delta = 6.3$	$\Delta = 1.2$	
$\theta = 15°$	19		22	17	
$\psi = 45°$	25		30	28	
	71		69	74	
	138		136	138	
			$\Delta = 3.1$	$\Delta = 2.3$	
$\theta = 20°$	17		24	16	
$\psi = 45°$	29		39	28	
	77		70	78	
			$\Delta = 8.1$	$\Delta = 1.0$	
$\theta = 6°$	24		20		20
$\psi = 0°$	48		43		46
	68		67		67
	129		126		134
			$\Delta = 3.6$		$\Delta = 3.4$
$\theta = 10°$	25				21
$\psi = 0°$	44				51
	72				70
	138				$\Delta = 4.2$

[a] The energy scale used in Ref. 25 is obtained by fitting to the work of Ref. 3 for $\theta = 6°$, $\psi = 45°$.

structure between 90 and 120 eV for the (10) beam. The description and reproducibility of details like this do not seem to be reliable at the present state of the art in both theory and experiment. Therefore, one should not be surprised if experiment gives a peak-shoulder combination and theory predicts a shoulder-peak combination. Also, note that with regard to peak positions the experiments can disagree to within easily 3–5 eV. These effects may be attributed to the different location in energy of the Bragg envelope that overlies the multiple-scattering structure.[16] The position of this envelope can be a sensitive function of the surface geometry for small values of λ_{ee}.[14,16] Consequently, in analyzing experimental data one must either average the experimental data in some way[37–39] to eliminate this problem or analyze large amounts of data and look for trends as we are doing here.

Although we have tried to be as quantitative as possible in discussing the degree of agreement between theory and experiment, criteria such as peak shape and the correspondence between peaks in different intensity profiles will always be highly subjective. This is particularly unfortunate in the case of Al (100) on which there has been a substantial amount of experimental[3–5] and theoretical[9–12,14,17,25] work that we would like to compare. One possible way to make more quantitative a comparison between different works is to simply compare the energies of the maxima of corresponding peaks in the profiles. As a measure of the degree of correspondence between two intensity profiles one could calculate the rms deviation between the positions of the prominent peaks in the profiles, i.e.,

$$\Delta = \left(\frac{1}{N} \sum_{j=1}^{N} (E_j^{(1)} - E_j^{(2)})^2 \right)^{1/2} . \tag{3.1}$$

In Eq. (3.1), "j" is the index labeling corresponding peaks in intensity profiles "1" and "2."

In Table I, we tabulate the positions of the maxima of some of the prominent peaks in several experimental and theoretical intensity profiles for the specular beam on Al (100). A "prominent" peak is simply one which exhibits a well-defined presence in all of the profiles. The rms deviations of the theoretically predicted peak positions from their experimental counterparts are also indicated. In determining the peak positions we simply took the energy at which the peak maximum occurred rather than attempting to determine the position of the "center of mass" of the peak. It is interesting to note that the theoretical calculations of Jepsen *et al.*[25] show very good correspondence to the experimental work of Jona[3] but not that of Farrell and Somorjai.[4] However, the details of the peak shapes and the secondary structure are degraded significantly at the larger angles of incidence. It is somewhat misleading to compare the predicted peak positions of Jepsen *et al.*[25] with the predicted peaks positions of this paper and the work of Tong and Rhodin[10] since Jepsen *et al.*[25] used no fixed energy zero but simply rigidly shifted the calculated profiles in order to obtain the best correspondence with Jona's work.[3]

The positions of several of the prominent peaks for the $(0\bar{1})$ beam are shown in Table II. It is significant to note that the degree of correspondence of the experimental work of Farrell and Somorjai[4] and of Burkstrand and Propst[5] with Jona's experimental work[3] is of the same order as the degree of correspondence of the theoretical calculations to Jona's work.[3] This perhaps is representative of the state of the art of both theory and experiment.

Table III gives the positions of several of the prominent peaks for the $(\bar{1}\bar{1})$ beam. There appears

TABLE II. Comparison between experimentally observed and theoretically prominent positions of the principal peaks (given in eV) in the LEED profiles for the $(0\bar{1})$ beam on Al(100).

	Experimental			Theoretical	
	Ref. 3	Ref. 4[a]	Ref. 5[a]	This work	Ref. 25
$\theta=0°$	56	55	54	50	56
	84	74	75	73	79
	105	98	107	102	105
		$\Delta=7.1$	$\Delta=5.4$	$\Delta=7.4$	$\Delta=2.9$
$\theta=6°$	59			50	64
$\psi=45°$	110			105	110
				$\Delta=7.3$	$\Delta=3.5$
$\theta=15°$	60			56	61
$\psi=45°$	116			112	115
				$\Delta=4.0$	$\Delta=1.0$
$\theta=20°$	39			29	26
$\psi=45°$	67			58	65
	125			111	125
				$\Delta=12.5$	$\Delta=7.6$

[a] Δ is defined relative to the peak positions of Ref. 3.

to be a better correspondence between theory and experiment for this beam than for the $(0\bar{1})$ beam. Again note that the degree of correspondence between the various experimental measurements[3-5] is of the same order as the correspondence of the theoretical calculations to any of the experiments.

In general, the model calculations seem to give an adequate qualitative description of the experimental LEED profiles from Al (100). However, the agreement between theory and experiment becomes generally poorer at the larger angles of incidence and the origin of the difficulties with the $(0\bar{1})$ beam (Fig. 1) is not known. Also, as a general trend the experimental peaks tend to lie somewhat higher in energy than the theoretical peaks. Finally we note that in view of the lack of detailed correspondence between different experimental works,[3-5] discrepancies of order 5 eV between theoretically predicted peak positions and a given experimental measurement simply are not meaningful.

IV. ALUMINUM (110)

An interesting feature of the (110) face of aluminum is that its small interlayer spacing makes structure associated with the $n=1$ Bragg peak observable (although, at these very low energies our value of λ_{ee} is almost certainly too small[15]). As in the case of the (100) face, we take as our model of the surface simply a truncated periodic bulk solid.

In Fig. 7, we show a comparison between the results of model calculations for the specular beam and the experimental work of Marsh[6] and of Jona.[3] The azimuth $\psi=90°$ corresponds to the beam being parallel to the long axis of the primitive rectangular two-dimensional cell of the surface.[3] The important feature of this figure is that the experimental peaks consistently lie 10–15 eV higher in energy than their theoretical counterparts. There is generally good agreement with respect to peak positions between the work of Marsh[6] and of Jona[3] except for the highest-energy peak which Marsh puts at 156 eV and Jona puts at 164 eV. Marsh's data show the peaks superposed on an increasing background. Evidently his work has not been normalized to unit incident beam current.

There also is little correspondence between theory and experiment regarding the qualitative features of the intensity profiles, i.e., features such as peak shape and relative peak heights. In particular, the work of Jona[3] shows a very prominent peak at ~ 28 eV, and the position of this peak is essentially independent of angle of incidence. This latter fact suggests the identification of the peak as a secondary peak caused by an intralayer multiple-scattering resonance rather than as a Bragg peak.[15,16] The model calculation gives only a small secondary peak near this position with the $n=1$ Bragg peak being the peak at ~ 2 eV. The disagreement between theory and experiment as regards the magnitude of the secondary peak is somewhat surprising since there was certainly a rough agreement in the magnitudes of the profiles near 30 eV for Al (100). This serious disagreement in peak size cannot be attributed to an unreasonable estimate of λ_{ee} [because of the correspondence

TABLE III. Comparison between experimentally observed and theoretically predicted positions of the prominent peaks (given in eV) in the LEED profiles for the $(\bar{1}\,\bar{1})$ beam on Al(100).

	Experimental			Theoretical	
	Ref. 3	Ref. 4[a]	Ref. 5[a]	This work	Ref. 25
$\theta=0°$	46		43	40	46
	90	88	86	84	91
	151	143	152	148	
		$\Delta=5.8$	$\Delta=2.9$	$\Delta=5.3$	$\Delta=0.7$
$\theta=6°$	39			41	45
$\psi=45°$	84			81	87
	149			145	
				$\Delta=3.1$	$\Delta=4.7$
$\theta=15°$	37			34	43
$\psi=45°$	84			80	85
	149			145	
				$\Delta=3.7$	$\Delta=4.3$
$\theta=20°$	38			38	39
$\psi=45°$	82			79	85
	50			153	
				$\Delta=2.4$	$\Delta=2.2$

[a] Δ is defined relative to the peak positions of Ref. 3.

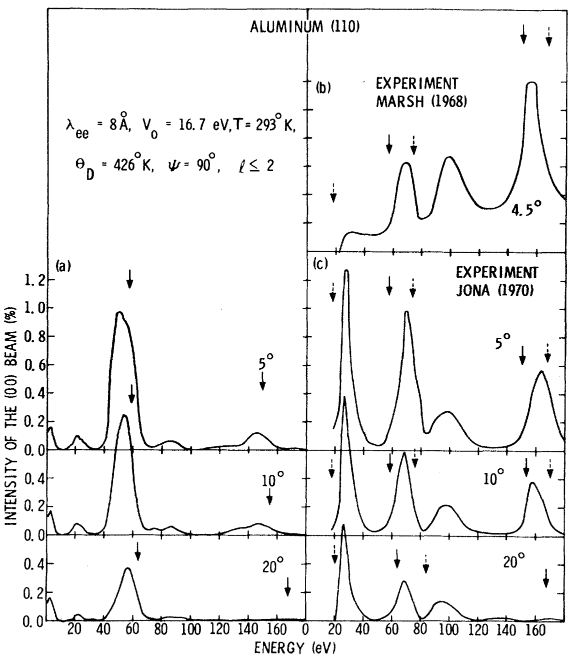

FIG. 7. Comparison between (a) the predictions of model calculations for the (00) beam, (b) the experimental work of Marsh (Ref. 6), and (c) of Jona (Ref. 3). The azimuthal angle is $\psi = 90°$ and the curves are labeled according to the polar angle θ. $\psi = 90°$ corresponds to the beam lying along the long axis of the two-dimensional rectangular unit cell (Ref. 3). The model calculations are based on the parameters indicated in the figure. The solid arrows and the dotted arrows mark the kinematical positions of the Bragg peaks using $V_0 = 16.7$ and 0 eV, respectively. The theoretical calculations are for the absolute reflectivity. The units of the experimental curves are arbitrary.

with Al (100)] or to the importance of partial waves for $l > 2$ (see Fig. 1). The absence of this peak in Marsh's work is presumably due to lack of incident beam intensity at this low energy. The theoretical calculation also underestimates the prominent secondary structure in the experimental profiles near 100 eV. This is not surprising, however, as it also underestimated the secondary structure near this energy for Al (100).

A comparison between theory and experiment for nonspecular beams at non-normal incidence is shown in Fig. 8. The agreement between theory and experiment is poor. To the extent that one can make a correspondence between theoretical and experimental peaks, the experimental peaks again appear to lie 10–15 eV higher in energy than their theoretical counterparts. In the case of the $(\bar{1}\bar{1})$ beam there is structure near 30 eV that lies very close to the kinematical position of a Bragg peak for zero inner potential. It has no apparent counterpart in the theoretical calculations which use an inner potential of 16.7 eV.

We finally turn to the case of normal incidence for which the agreement between theory and experiment is best in the case of Al (100). The comparison between theory and experiment for the case of normal incidence is shown in Fig. 9. For purposes of estimating the dependence of the profiles on small changes in the angle of incidence at nearly normal incidence, the (00) beam is also plotted. Comparison of this plot with the curve for $\theta = 5°$ in Fig. 7 shows only minor changes. In the case of the (10) beam the clusters of multiple-scattering peaks in the experimental work lie about 16 eV higher in energy than the corresponding clusters in the model calculations. In the case of the (01) beam the agreement between theory and experiment is such that it is difficult to say anything definitive. However, the experimental peaks do appear to lie of order ~10 eV above the theoretical peaks. For the (11) beam the centers of the ex-

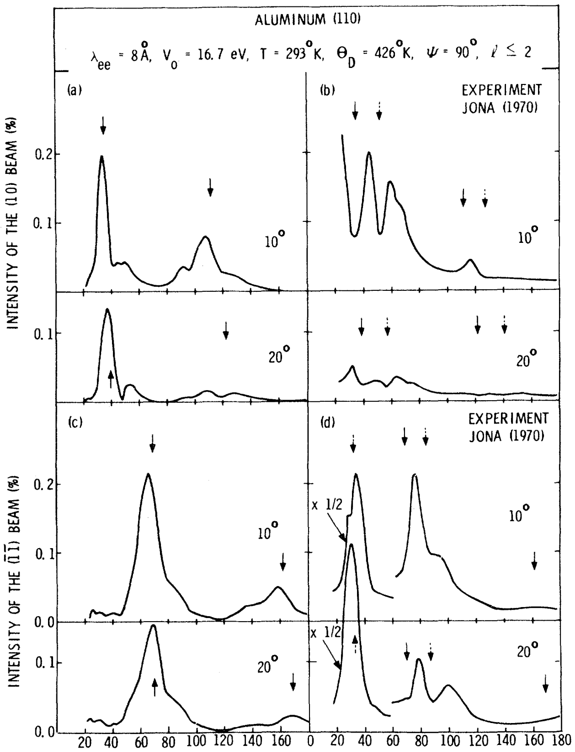

FIG. 8. Comparison between (a) and (c) the predictions of model calculations and (b) and (d) Jona's experimental work (Ref. 3) for the (10) and the $(\bar{1}\,\bar{1})$ beams. $\psi = 90°$ corresponds to the beam being parallel to the long axis of the two-dimensional rectangular unit cell (Ref. 3). The model calculations use the parameters indicated in the figure with the curves being labeled according to the polar angle θ. The solid arrows and the dotted arrows mark the kinematical positions of the Bragg peaks using $V_0 = 16.7$ and 0 eV, respectively. The theoretical calculations are for the absolute reflectivity. The units of the experimental curves are arbitrary.

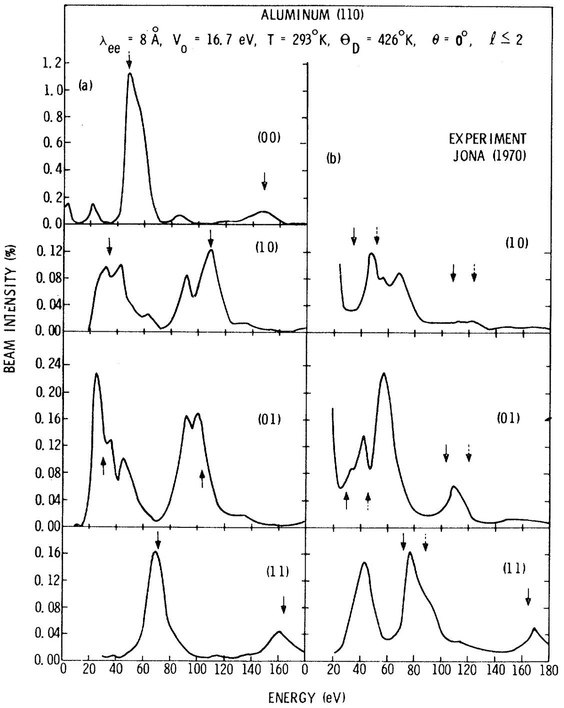

FIG. 9. Comparison between (a) the predictions of model calculations and (b) Jona's experimental work (Ref. 3) for the case of a normally incident beam. Model calculations are based on the parameters indicated in the figure. The solid arrows and the dotted arrows mark the kinematical positions of the Bragg peaks using $V_0 = 16.7$ and 0 eV, respectively. The theoretical calculations are for the absolute reflectivity. The units of the experimental curves are arbitrary.

perimental clusters appear to lie 8–10 eV higher than their theoretically predicted positions.

Summarizing the results of the comparison of the model calculations and data for Al (110), the peaks in the experimental intensity profiles appear to lie consistently of order 10–15 eV higher in energy than the peak positions predicted treating the surface as if it were a truncated bulk solid. Yet this model adequately describes the data for Al (100). This anomalous behavior of Al (110) was noted in earlier work using the phenomenological isotropic-scatterer version of the inelastic collision model[14] for both the $\psi = 0°$ and $90°$ azimuth. The $\psi = 0°$ azimuth has been investigated for $\theta = 5°$ using higher partial waves[9] with the results being very similar to the $\psi = 90°$ azimuth. There also is poor qualitative agreement between the model predictions and the experimental results with respect to peak shape and relative peak intensities. Possibly the problem may be due to surface contamination of the (110) face. Because of its "loosely packed" character, the (110) face of an fcc material can be more reactive than the (100) and the (111) faces. However, even for a chemically clean "flat" surface, peak shifts of order 10 eV can be produced by distortions of order 10% in the spacing between the top two layers of the solid.[14] This point will be discussed in more detail in Sec. VI where we consider the various ways a chemically clean surface can be inequivalent to simply a trucated bulk solid.

V. ALUMINUM (111)

The layer spacing of Al (111) is somewhat larger than that of Al (100). Consequently, analogous features in the intensity profiles occur at lower energies for Al (111) than for Al (100). As in the case of the (100) and the (110) faces, we take as our model of the surface a truncated bulk solid.

A comparison between the results of model calculations for the specular beam and the experimental work both of Porteus and Faith[7] and of Jona[3] is shown in Fig. 10. The work of Jona[3] is on single-crystal aluminum, while the work of Porteus and Faith[7] is on an Al (111) surface epitaxially grown on a Si (111) single-crystal surface. On the (111) face there is a potential ambiguity between the azimuths $\psi = 0°$ and $60°$, but because of reciprocity[40] the profiles for both azimuths should be identical. Outside of minor differences in the intensity profiles, Jona's experimental work bears this out.[3] We use Jona's definition of the azimuthal angle[3] and in our model calculations use the layer stacking sequence specified by Nicholas.[41] Comparing first Jona's results with the model predictions we see that for $\theta = 5°$ the experimental peaks are ~10 eV higher in energy than the corresponding theoretical peaks. For $\theta = 15°$ the experimental peaks are of order 7 eV higher in energy than the corresponding theoretical peaks. For both $\theta = 5°$ and 15° the low-energy peaks at ~20 eV are much larger in the experimental curves than in the theoretical curves. This structure is associated with the $n = 2$ Bragg peak. The reason for discrepancy in size probably is due to the use of too small a value of λ_{ee} in the theoretical calculations in this energy range.[15] However, for $\theta = 25°$ excellent agreement exists between theory and experiment for the low-energy peak at ~ 12 eV. The model calculation predicts a cluster of multiple-scattering peaks between 30 and 70 eV. The experimental work also indicates this cluster but the center peak is much more prominent than the other peaks in the cluster. The agreement as regards peak shape hence is poor.

Porteus and Faith[7] were interested primarily in inelastic electron diffraction and so they measured the elastic energy profile at only one angle of incidence. Their work puts the clusters of peaks at the Bragg energies at ~50 and ~100 eV in agreement with the predictions of the model calculations. The corresponding peaks in Jona's work are ~8 eV

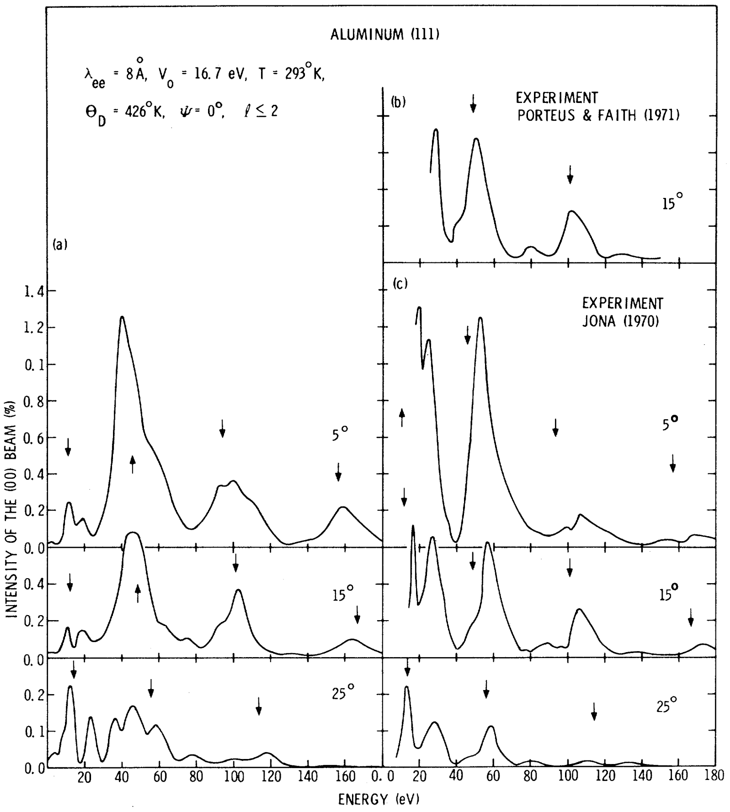

FIG. 10. Comparison between (a) the predictions of model calculations for the (00) beam and (b) the experimental work of Porteus and Faith (Ref. 7) and (c) of Jona (Ref. 3). The model calculations use the parameters indicated in the figure with the curves being labeled according to the polar angle θ. The solid arrows mark the kinematical positions of the Bragg peaks using $V_0 = 16.7$ eV. The theoretical calculations are for the absolute reflectivity. The units of the experimental curves are arbitrary.

higher in energy. The lowest peak in the Porteus and Faith curve occurs at ~29 eV which is in agreement with Jona's work and ~8 eV higher than the theory predicts.

In Fig. 11, we show a comparison between the results of model calculations and the experimental work of Jona[3] for the $(\bar{1}\,\bar{1})$ beam taken at the $\psi = 60°$ azimuth. For $\theta = 0°$ there is a correspondence between the theoretical and the experimental peaks, but the experimental peaks lie ~5 eV higher in ener-

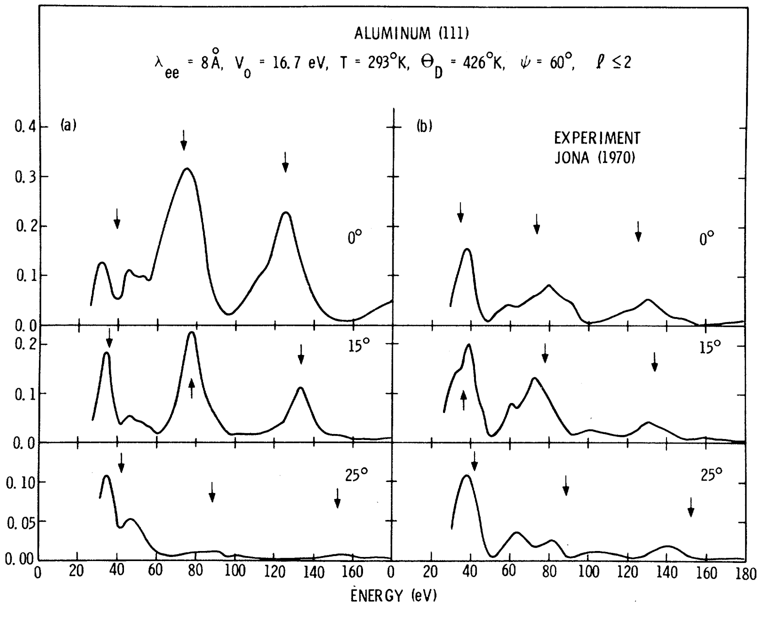

FIG. 11. Comparison between the predictions of model calculations for (a) the $(1\bar{1})$ beam and (b) Jona's experimental work (Ref. 3). The model calculations are based on the parameters indicated in the figure with the curves being labeled according to the polar angle θ. The solid arrows mark the kinematical positions of the Bragg peaks using $V_0 = 16.7$ eV. The theoretical calculations are for the absolute reflectivity. The units of the experimental curves are arbitrary.

gy than their theoretical counterparts. At $\theta = 15°$ there is agreement with respect to peak positions but rather poor agreement as to the over-all shapes of the peaks. The theory gives a secondary peak at ~45 eV while the experimental data shows a shoulder at this energy. At $\theta = 25°$ the agreement between theory and experiment with respect to peak shapes is sufficiently poor that it is difficult to say much regarding peak positions beyond the fact that both theory and experiment give a prominent peak near 35 eV.

We cannot propose any definitive conclusions for Al (111) because of the difference in peak position of order 5 eV when one compares the available experimental work.[3,7] Across the range of the considered data, the experimental peak positions differ from the theoretical peak positions only of order 5 eV. As the uncertainty in the experimental data also is of this magnitude, a charitable reader might conclude that the model calculations appear to provide a reasonable description of the experimental data for Al (111).

VI. EFFECT OF SPECIFICALLY SURFACE PHENOMENA ON INTENSITY PROFILES

In Secs. III–V, we compared experimental LEED profiles with the results of model calculations which treated the surface as if it were simply a truncated but otherwise perfectly periodic "bulk" material. This is not expected to be the case for real materials.[18,19,42] However, such a comparison is the necessary first step in using LEED to learn about surface properties. The model calculations are highly simplified, of course, in that they neglect threshold effects that may be quite important when the electron energy is near the plasmon energy[36] and treat the consequences[13,36,42,43] of the long-range nature of the electron-solid interaction in an *ad hoc* way. Both the model calculations and the experimental measurements are extremely sensitive to the properties of the first two or three atomic layers of the solid which may be quite different from those in the bulk.[2,13–17,42] In particular, the ion cores in the surface layer may be electronically, vibronically, and geometrically inequivalent to the ion cores in the "bulk" region of the solid. In this section we discuss the consequences of these types of inequivalence on the intensity profiles.

The term electronic inequivalence indicates that the surface ion cores exhibit different electron scattering properties from the bulk ion cores. This effect has been extensively investigated using the phenomenological isotropic-scattering version of the inelastic-collision model.[2,13–16] An electronic inequivalence primarily alters the secondary structure in the intensity profiles and has little effect upon the predominant structure near the kinematical Bragg energies (apart from an over-all scale change in the profiles). Specifically, increasing the scattering strength of the surface ion cores relative to the "bulk" ion cores enhances the relative importance of the secondary structure, and decreasing the scattering strength of the surface relative to the bulk leads to kinematiclike intensity profiles. The insensitivity of the positions of the clusters of peaks near the primary Bragg energy to the details of the electron–ion-core potential is illustrated in Fig. 2.

The effect of a vibronic inequivalence of the surface layer has been investigated in some detail within the framework of the *s*-wave model.[2,14] As the rms displacements of the ion cores from their equilibrium position increases (which occurs near the surface)[2,18,19,30–32] the effective electron–ion-core scattering amplitude becomes concentrated in the forward direction. This result is evident from Eqs. (2.24) and (2.25). Thus the single-scattering contribution of the surface layer to the backscattered LEED intensity is decreased. This diminution reduces the intensity of the peaks in the intensity profiles and, since the effect is exponentially dependent on the energy, it affects the higher-energy peaks more strongly than the lower energy peaks. The phenomenon is described in detail in Ref. 2 where it was concluded that although all experimental data indicate that the surface ion cores have a larger amplitude of vibration than the bulk ion cores, it is not possible to extract quantitative information about the rms vibrational amplitudes unless the electronic properties of the system are also known. Such a process requires analyzing large blocks of data at different temperatures in a self-consistent way in order to obtain both the electronic and the vibrational properties.[14] The result that is important for our present discussion is that if the equilibrium positions of the ion cores are fixed, changes in the vibrational properties can at best shift peak positions by a few tenths of an eV.

In order to rationalize discrepancies between the predicted and measured peak positions of the order of those observed on Al (110), we must examine the effects of a geometrical inequivalence of the surface layer.[14] By a geometrical inequivalence we mean that the equilibrium positions of the ion cores are not the same as those in a corresponding truncated "bulk" solid. Even if the geometry of the individual atomic layers is unaffected near the surface, theoretical calculations based upon two-body force models indicate that spacings between adjacent layers are several percent larger than the spacings in the bulk.[18,19] However, there have been suggestions by Germer and co-workers[44–47] that experimental LEED data indicates a contraction in the upper layer spacing of Ni (110) and

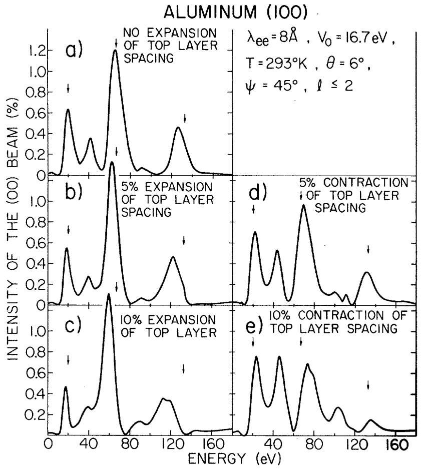

FIG. 12. Effect of various distortions of the upper-layer spacing on the calculated intensity profiles of the (00) beam on Al (100). The model calculations are for the absolute reflectivity. They are based on the parameters indicated in the figure. The arrows mark the kinematical positions of the Bragg peaks using $V_0 = 16.7$ eV.

W (110). In an earlier work[14] we specifically investigated the effect of a change in the upper-layer spacing using the phenomenological isotropic-scatterer version of the inelastic-collision model and found that there could be both appreciable shifts in peak position and distortions in peak shape for 5–10% changes in the upper-layer spacing. These effects persist when higher partial waves are incorporated into the calculation.

In Fig. 12, we show the effect on the intensity profiles of varying degrees of distortion of the top-layer spacing for Al (100). The distortion of the upper-layer spacing produces both a shift in peak position and a modulation in the peak intensities. A discussion of these effects in the kinematic limit is given by Duke *et al.*[14] so we do not repeat it here. An expansion of the upper-layer spacing shifts peaks to lower energies and produces low-energy shoulders on the peaks. Conversely, a contraction of the upper-layer spacing shifts peaks to higher energies and produces high-energy shoulders on the peaks. The production of shoulders on the peaks is more pronounced when only *s*-wave phase shifts are used in the calculation.[14] The intensity of the secondary structure also depends strongly on the upper-layer spacing. In particular, it increases dramatically when the upper-layer spacing is contracted. Notice that shifts in peak positions of order 10 eV easily can be obtained for 10% changes in the upper-layer spacing.

Recalling from Sec. IV that the main discrepancies between the model predictions and the experimental intensities on Al (110) were that the experimental peaks are 10–15 eV higher in energy than the theoretical peaks and that the secondary structure in the experimental profiles was much more pronounced than in the theoretical profiles, we look at the effects of a contraction of the upper-layer spacing on the calculated intensity profiles from Al (110). The results of sample calculations are shown in Fig. 13 where γ specifies the degree of distortion of the upper-layer spacing, i.e.,

$$d' = (1+\gamma)\,d, \tag{6.1}$$

where d' is the upper-layer spacing and d is the undistorted "bulk"-layer spacing. In panels (a)–(d) of the figure the amount of contraction of the upper-layer spacing is continually increased keeping the effective electron mean-free-path constant. For a 15% contraction of the upper-layer spacing [panel (c)], the intensity of the secondary peak near 25 eV has increased noticeably and the position of the $n = 2$ Bragg peak has shifted approximately 10 eV upward in energy. The secondary structure near 80 eV has been enhanced and distorted by the contraction. More partial waves would have to be incorporated into the calculation in order to draw definitive conclusions about secondary structure in this energy range. An attempt to cause still further peak motion to higher energies by a greater contraction of the upper-layer spacing is shown in Fig. 13(d). In Fig. 13(e) we show that for a smaller effective mean free path the same degree of peak motion can result for a smaller change in the upper-layer spacing—compare panels (c) and (e). The effect of uncertainties in λ_{ee} on the extraction of quantitative information about the amount of distortion of the upper-layer spacing is discussed later in this section. Here we merely note that a contraction of the upper-layer spacing causes the sort of qualitative changes in the intensity profiles required to account for the differences between the theory predictions and experiment measurements for Al (110).

Figure 14 illustrates another manifestation of a distortion of the upper-layer spacing. As the angle of incidence is increased, the clusters of peaks near the Bragg energies move to higher energies as evidenced by the motion of the arrows in Fig. 14. The effect of an expansion of the upper-layer spacing is to slow down the peak motion relative to the kinematical Bragg positions. Conversely, the effect of a contraction of the upper-layer spacing is to speed up the motion of the peaks relative to the kinematical Bragg positions. The effect of a change in the upper-layer spacing on the secondary structure appears greater at the large angles of incidence. Also note that there is no formation of the doublet structure near 20 eV with increasing angle of incidence for the case of a 7% expansion of the upper-layer spacing. The systematic formation of the doublet is observed experimentally

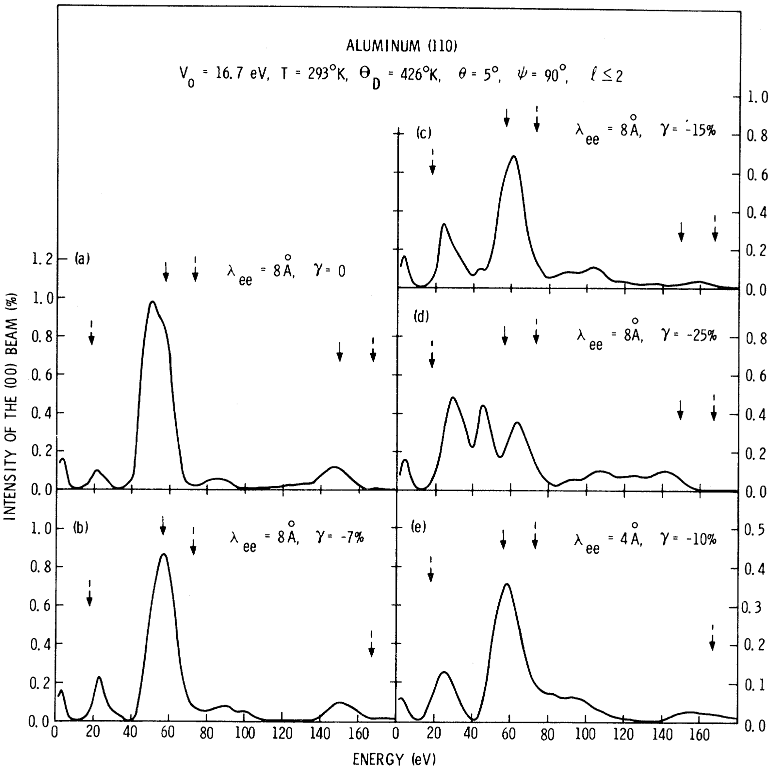

FIG. 13. Effect of a contraction of the upper-layer spacing on the calculated intensity profiles of the (00) beam on Al (110). Model calculations are for the absolute reflectivity and use the parameters indicated in the figure. In panels (a)–(d) λ_{ee} = 8 Å and in panel (e) λ_{ee} = 4 Å. The solid arrows and the dotted arrows mark the kinematical positions of the Bragg peaks using V_0 = 16.7 and 0 eV, respectively. The upper-layer spacing d' is specified in terms of the undistorted bulk-layer spacing d through $d' = (1+\gamma)\,d$.

(Fig. 3) and is present in the calculated profiles for $\gamma = 0$ and $\gamma = -7\%$.

Uncertainties in both the angular dependence and the magnitude of the self-energy[13,26,27] make it difficult to extract quantitative information about the degree of a distortion of the upper-layer spacing on the basis of peak energies in the experimental intensity profiles. Using the highly simplified model for Σ given in Eqs. (2.38) and (2.39) it is clear that we could account for a part of the peak shift by treating V_0 as a parameter which depends on the angle of incidence and the energy. As indicated in Fig. 13 the actual amount of peak motion for a given distortion of the upper spacing depends on the effective penetration of the elastic wave field of the electrons into the solid. We can estimate the magnitude of the uncertainties introduced by this effect within the context of our model of Σ by examining the amount of peak motion for various values of λ_{ee}. Such an examination is shown in Fig. 15 for the $n = 3$ Bragg peak of the (00) beam from Al (100). The results both of isotropic-scatterer calculations[14] and of calculations using the $l \leq 2$ partial waves of Fig. 1 are shown in the figure. These two types of calculations give identical results. The range of values 4 Å $\leq \lambda_{ee} \leq$ 12 Å represents what seems to us to be reasonable limits for λ_{ee} in the energy range shown in Fig. 15. For a 10% change in the upper-layer spacing the change in peak position due to variation in λ_{ee} is of order 5 eV. It is hence unreasonable to try to interpret variations in peak positions of this magnitude. The 10–15-eV discrepancies in peak positions observed for Al (110) are outside this uncertainty.

Finally, we remark that although uncertainties in the behavior of $\Sigma(\vec{k}, E)$ can cause substantial uncertainties in the interpretation of experimental data, we expect it to behave the same way as a function of the beam parameter E and θ for all faces of a given material (provided that the faces are free from contamination). Thus, anomalies in the ex-

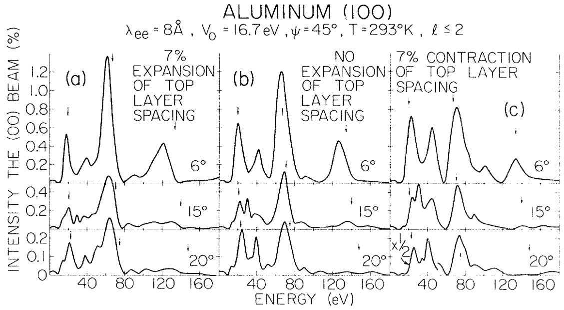

FIG. 14. Effect of a distortion of the upper-layer spacing on the change in peak position with angle of incidence. The model calculations are for the absolute reflectivity of the (00) beam from Al (100) and are based on the parameters indicated in the figure. Curves are labeled according to the polar angle θ. The arrows mark the kinematical positions of the Bragg peaks using V_0 = 16.7 eV.

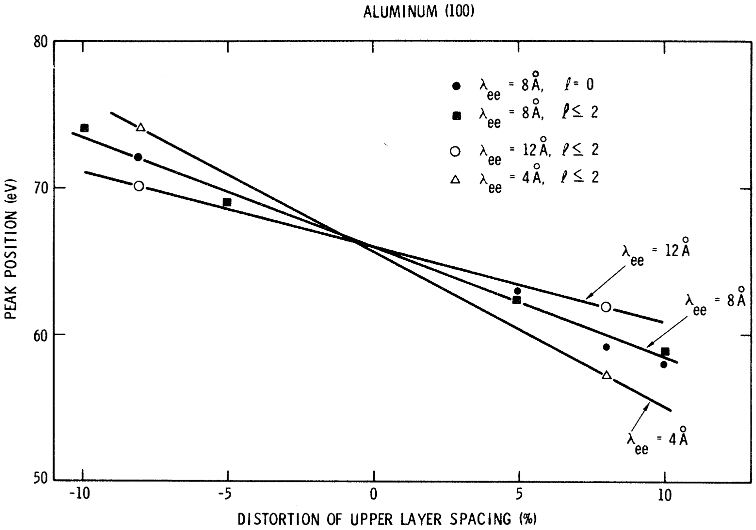

FIG. 15. Position of the $n=3$ Bragg peak of the specular beam from Al (100) as a function of both the distortion of the upper-layer spacing and the effective electron mean free path ($\lambda_{ee}=2\lambda_{mfp}$). The parameters used in the calculations were $V_0=16.7$ eV, $\theta=6°$, $\psi=45°$, $\Theta_D=426°$ with the results of both isotropic-scatterer calculations (Ref. 14) and calculations involving the higher partial waves of Fig. 1 being shown in the figure. The upper-layer spacing is expressed in terms of the bulk-layer spacing and as indicated in Eq. (6.1). There are points for all three curves at $\gamma=0$, $E=66$ eV. For purposes of clarity these points are not shown in the figure.

perimental data taken from different "clean" faces of the same material should indicate different surface properties of these faces.

VII. SUMMARY AND CONCLUSION

In this paper we used a version of the inelastic-collision model[48] which incorporated both the effects of lattice vibrations[1,2] and a "realistic" model of the electron–ion-core potential[8] to analyze LEED data from the (100), (110), and the (111) faces of aluminum. Reflectivity boundary conditions were used in order to obtain an absolute value of the reflectivity from the calculation. As a necessary first step in extracting specifically surface properties from the LEED data, the model calculations treated the surface as if it were simply a truncated but otherwise perfectly periodic idealized bulk solid. This model was found to adequately describe the data from Al (100). The description of the data was less satisfactory for Al (111). However, the disagreement between the model predictions and experimental intensities was not great enough to extract any meaningful information concerning distorted surface geometry at the present state of the art of both theory and experiment. In the case of Al (110) there is a clear anomaly: The peaks in the intensity profiles consistently occur 10–15 eV higher in energy than the corresponding peaks in the model calculations. If the surface is assumed to be "flat" and free from contamination, it was found that only a *contraction* of the upper-layer spacing of the (110) face *of order* 10% could account for this result. To ensure that the surfaces in question really are chemically clean, the experiments need to be repeated in conjunction with an independent monitor of surface chemical composition.[20,21]

This summary brings us back to a question raised in the Introduction: How accurate a description of experimental LEED intensities is possible in light of our rudimentary understanding of the electron-solid force law for electrons in the energy range 10 eV $\leqslant E \leqslant$ 1000 eV? All of the geometrical information about the (100) and (110) faces of aluminum, including the possibility of a contracted (110) outer-layer spacing, already was inferred from our schematic s-wave model analysis.[14] The use of a more refined short-range electron-ion-core interaction undoubtedly improves the prediction of the absolute intensities of the scattered beams.[9,12] However, the neglect of the long-range interaction between the incident electron and its induced surface charge renders our model description of these intensities qualitative at best.[13,27] At small angles of incidence, the intensity profiles predicted by the present microscopic model indeed "appear" to be in better agreement with experiment than those of the schematic s-wave model.[14] However, at $\theta \gtrsim 20°$ even the visual resemblance between the model predictions and the data deteriorates. The detailed prediction of the energies and intensities of the secondary peaks between the clusters of peaks near the Bragg energies is never really satisfactory. In short, both our present calculation with a microscopic model of the electron–ion-core interaction and the schematic s-wave model adequately describe the energies of the prominent clusters of peaks near the Bragg energies. Although the present calculation gives a noticeable improvement in the over-all intensities and visual appearance of the predicted intensities at small angles of incidence, it still does not provide a quantitative description of the data. We do not know whether this shortcoming is caused by inadequate sample characterization (i.e., our model of the actual surface condition is inapplicable), by our ignorance of the electron-solid force law, by inadequate knowledge of the experimental response function, or by all three. However, it seems accurate to conclude that in the case of geometrical effects both models provide adequate descriptions of large effects, whereas neither model provides a truly convincing description of the finer details (whether electronic, vibronic, or geometrical in origin) of the observed intensity profiles.

Note added in proof: The curves of Burkstrand and Propst shown in Fig. 6 represent preliminary work and subsequent measurements have led to minor changes. The peak positions given in Tables II and III are for the final versions of the experimental curves.

ACKNOWLEDGMENTS

We would like to thank J. M. Burkstrand and F. M. Propst for allowing us to show their unpublished data on Al (100), and J. O. Porteus and W. N. Faith for allowing us to show their unpublished data on Al (111). We would also like to acknowledge the assistance of A. B. Kunz in obtaining the phase shifts used in this work.

[†] Work supported in part by the U. S. Atomic Energy Commission, in part by the Advanced Research Agency under Contract No. HC-15-67-C-0221, and in part by the Air Force Office of Scientific Research, Office of Aerospace Research USAF under Grant No. AFOSR-71-2034. The United States Government is authorized to reproduce and distribute reprints for Governmental purposes notwithstanding any copyright notation hereon.

[1] C. B. Duke and G. E. Laramore, Phys. Rev. B 2, 4765 (1970).

[2] G. E. Laramore and C. B. Duke, Phys. Rev. B 2, 4783 (1970).

[3] F. Jona, IBM J. Res. Develop. 14, 444 (1970).

[4] H. H. Farrell and C. A. Somorjai, Phys. Rev. 182, 751 (1969).

[5] J. M. Burkstrand and F. M. Propst (private communication).

[6] J. B. Marsh, General Electric TIS Report No. 68-C-287, 1968 (unpublished). This work also appears in Fig. 13 of Ref. 15.

[7] J. O. Porteus and W. N. Faith, (a) in Proceedings of the Fifth Low-Energy Electron Diffraction Seminar, 1971 (unpublished); (b) and private communication.

[8] E. C. Snow, Phys. Rev. 158, 683 (1967).

[9] G. E. Laramore, C. B. Duke, A. Bagchi, and A. B. Kunz, Phys. Rev. B 4, 2058 (1971).

[10] S. Y. Tong and T. N. Rhodin, Phys. Rev. Letters 26, 711 (1971).

[11] V. Hoffstein and D. Boudreaux, Phys. Rev. Letters 25, 512 (1970); Phys. Rev. B 3, 2447 (1971).

[12] J. A. Strozier, Jr. and R. O. Jones, Phys. Rev. Letters 25, 516 (1970); Phys. Rev. B 3, 3228 (1971).

[13] C. B. Duke and C. W. Tucker, Jr., Phys. Rev. B 3, 3561 (1971).

[14] C. B. Duke, C. E. Laramore, B. W. Holland, and A. M. Gibbons, Surface Sci. (to be published).

[15] C. B. Duke, J. R. Anderson, and C. W. Tucker, Jr., Surface Sci. 19, 117 (1970).

[16] C. W. Tucker, Jr. and C. B. Duke, Surface Sci. 24, 31 (1971).

[17] C. B. Duke, A. J. Howamon, and G. E. Laramore, J. Vac. Sci. Technol. 8, 10 (1971).

[18] R. E. Allen and F. W. deWette, Phys. Rev. 179, 873 (1969).

[19] R. E. Allen, F. W. deWette, and A. Rahman, Phys. Rev. 179, 887 (1969).

[20] E. N. Sickafus and H. P. Bonzel, in *Recent Progress in Surface Science*, edited by J. F. Danielli, K. G. A. Pankhurst, and A. C. Riddiford (Academic, New York, 1970).

[21] R. L. Park, J. E. Houston, and D. G. Schreiner, Rev. Sci. Instr. 41, 1810 (1970).

[22] K. Kambe, Z. Naturforsch. 22a, 422 (1967).

[23] See, for example, J. D. Jackson, *Classical Electrodynamics* (Wiley, New York, 1963), Chap. 3.

[24] See, for example, M. L. Goldberger and K. M. Watson, *Collision Theory* (Wiley, New York, 1965).

[25] D. W. Jepson, P. M. Marcus, and F. P. Jona, in Ref. 7 (a).

[26] A. Bagchi, C. B. Duke, and P. J. Feibelman, Program of the Thirty-First Physical Electronics Conference, 1971 (unpublished).

[27] C. B. Duke, G. E. Laramore, and C. W. Tucker, Jr., in Ref. 7 (a).

[28] In general, $k_\perp(\vec{g}, E)$ defined through Eq. (2.16) is complex. The sign of $\mathrm{Im}\,k_\perp(\vec{g}, E)$ is always chosen to make the integral converge, i.e., $\mathrm{Im}\,k_\perp(\vec{g}, E)$ is taken as positive for $z > 0$. The sign of $\mathrm{Re}\,k_\perp(\vec{g}, E)$ may be either positive or negative depending on whether we are dealing with a transmitted or a reflected wave.

[29] See, for example, C. Kittel, *Introduction to Solid State Physics* (Wiley, New York, 1963), Chap. 6.

[30] E. R. Jones, J. T. McKinney, and M. B. Webb, Phys. Rev. 151, 476 (1966).

[31] R. M. Goodman, H. H. Farrell, and G. A. Somorjai, J. Chem. Phys. 48, 1046 (1968).

[32] J. M. Morabito, Jr., R. F. Steiger, and G. A. Somorjai, Phys. Rev. 179, 638 (1969).

[33] *Handbook of Chemistry and Physics*, edited by R. C. West (Chemical Rubber Co., Cleveland, Ohio, 1970), p. D-135.

[34] The phase shifts were obtained by the standard technique of numerically integrating the radial part of the Schrödinger equation using the potential specified in Ref. 8. See for example, D. R. Hartree, *The Computation of Atomic Structure* (Wiley, New York, 1957).

[35] A. Goldsmith, T. E. Waterman, and H. J. Hirschborn, *Handbook of Thermophysical Properties of Solid Materials* (MacMillan, New York, 1961), Vol. I, p. 49.

[36] C. B. Duke and G. E. Laramore, Phys. Rev. B 3, 3183 (1971); 3, 3198 (1971).

[37] C. W. Tucker, Jr., and C. B. Duke, Surface Sci. 23, 411 (1970).

[38] C. B. Duke and C. W. Tucker, Jr., J. Vac. Sci. Technol. 8, 5 (1971).

[39] M. B. Webb in Ref. 7 (a); M. G. Lagally, T. C. Ngoc, and M. B. Webb, Phys. Rev. Letters 26, 1557 (1971).

[40] D. P. Woodruff and B. W. Holland, Phys. Letters 31A, 207 (1970).

[41] J. F. Nicholas, *Atlas of Models of Crystal Surfaces*

(Gordon and Breach, New York, 1965).

[42] C. B. Duke, Ann. Rev. Mater. Sci. (to be published).

[43] A. Bagchi, C. B. Duke, and P. J. Feibelman, Proceedings of the Thirty-First Physical Electronics Conference, 1971 (unpublished).

[44] L. H. Germer, A. U. MacRae, and C. D. Hartman, J. Appl. Phys. 32, 2432 (1961).

[45] L. H. Germer and A. U. MacRae, Ann. N.Y. Acad. Sci. 101, 605 (1963).

[46] A. U. MacRae and L. H. Germer, Ann. N. Y. Acad. Sci. 101, 627 (1963).

[47] J. W. May and L. H. Germer, J. Chem. Phys. 44, 2895 (1966).

[48] C. B. Duke and C. W. Tucker, Jr., Surface Sci. 15, 231 (1969).

PHYSICAL REVIEW B VOLUME 5, NUMBER 2 15 JANUARY 1972

Two-Phonon Response of Anharmonic Lattices in the First-Order Self-Consistent Phonon Approximation

N. R. Werthamer
Bell Telephone Laboratories, Murray Hill, New Jersey 07974

(Received 27 August 1971)

Further extensions are made to a previously developed analysis for the two-time correlation functions in anharmonic lattices within the first-order self-consistent phonon approximation. This stationary-variation approximation is shown to represent an energy minimum if and only if the one-phonon response is stable. An explicit expression is exhibited for the two-phonon response and is interpreted as yielding an effective interaction between phonons. It is shown that the first-order approximation is not fully adequate for describing transport properties (e.g., thermal conductivity) or for investigating resonances or bound states of the two phonons. The distortion of the one-phonon peak in the inelastic-neutron or Raman-scattering cross section due to the finite size of the momentum transfer is investigated in more detail than the previous analysis.

I. INTRODUCTION

In a previous publication[1] we studied the inelastic-coherent-neutron-scattering cross section from an anharmonic lattice and analyzed the interpretation of this cross section in terms of the spectral functions of the phonon vibrational modes of the lattice. Using this information we calculated the neutron cross section arising from the first-order self-consistent phonon approximation for the dynamics of the anharmonic lattice. From the expression for the cross section, the one-phonon propagator in this approximation was extracted.

It is also of substantial importance to obtain information about two-phonon propagation. In the first place, Raman scattering in quantum crystals with two-phonon emission[2,3] has been demonstrated to be an observable effect.[4] It needs for its interpretation an understanding of the extent to which such scattering measures merely a convolution of one-phonon spectra. Second, the deviation from such convolution represents an interaction between phonons, and so gives information about whether two phonons might attract each other sufficiently to produce a bound state or a resonance.[5] This question is of particular interest[6] in relation to neutron[7]- or light-scattering[8] experiments in superfluid liquid helium. Finally, the two-phonon propagator is an essential ingredient in a calculation of thermal transport from a linear-response-function approach.[9]

In the present paper we extend our existing formalism[1] to calculate the two-phonon propagator in the first-order self-consistent phonon approximation. By comparison with the convolution of two one-phonon propagators, an explicit expression is obtained for the interaction of two phonons. The phonons are found to interact directly, as well as indirectly, by the exchange of one or more other phonons. A number of vertex corrections emerge at this level of approximation. However, since the interaction does not iterate and the two phonons do not scatter multiply, the first-order approximation is not a fully adequate framework for a self-contained development of lattice thermal transport, and it also cannot definitely answer the question of the existence of bound or resonant two-phonon states.

We are also able, by the use of a more compact notation, to exhibit in a more precise form than previously[1] the leading interference terms between the one-phonon peak in the neutron- or light-scattering cross sections and the multiphonon background. Further insight is gained into the extent to which the one-phonon–multiphonon interference can distort the observed peak from the one-phonon spectral function.

II. DERIVATIONS

A. Functional Formalism

The most serious obstacle to presenting the